This article has been accepted for publication in a future issue of this journal, but has not been fully edited. Content may change prior to final publication. Citation information: DOI 10.1109/TWC.2021.3078808, IEEE Transactions on Wireless Communications

Mobility-Enhanced Simultaneous Lightwave Information and Power Transfer

Mingqing Liu, Mingliang Xiong, Qingwen Liu, *Senior Member, IEEE*, Shengli Zhou, *Fellow, IEEE*, and Hao Deng

***Abstract*—Simultaneous lightwave information and power transfer (SLIPT) has been regarded as a promising technology to deal with the ever-growing energy consumption and data-rate demands in the Internet of Things. We propose a resonant beam based SLIPT (RB-SLIPT) system, which deals with the conflict of high deliverable power and mobile receiver positioning with the existing SLIPT schemes. At first, we establish a mobile transmission channel model and depict the energy distribution in the channel. Then, we present a practical design and evaluate the energy/data transfer performance within the moving range of the RB-SLIPT. Numerical evaluation demonstrates that the RB-SLIPT can deliver more than 4W charging power and enable 3Gb/s achievable data rate with the moving range of 20° field of view (FOV) over 3m distance. Thus, RB-SLIPT can enable simultaneous high deliverable power and high data rate in mobile scenarios without tracking control.**

***Index Terms*—Simultaneous lightwave information and power transfer; Resonant beam system; Wireless power transfer; Mobility and self-alignment; Retro-reflective resonator**

I. Introduction

Simultaneous wireless information and power transfer has been regarded as one of the enabling technologies in 6th generation (6G) networks [1]. Due to the spectrum crisis of radio frequency (RF), the simultaneous lightwave information and power transfer (SLIPT) adopting light-emitting diode (LED) lights or lasers as carriers has become a promising alternative/complementary technology [2–4]. However, as in Fig. 1, the LED-based SLIPT faces challenges of low deliverable charging power [5, 6], and the laser-based SLIPT is difficult to position mobile receivers [7, 8]. Thus, we propose a resonant beam-based SLIPT (RB-SLIPT) scheme, which can deal with the conflict between high deliverable power and mobile receiver positioning. The RB-SLIPT system is capable of simultaneously providing multi-Watt charging power and high-rate data transfer with self-alignment capability over distances of several meters.

The RB-SLIPT system inherits the characteristics of the resonant beam system (RBS). RBS is essentially an open-cavity laser resonator, where a transmitter consists of a high-reflective mirror and a gain medium and a receiver consists of an output coupling mirror and a Photovoltaic (PV) cell are spatially separated to form a resonator [9–11]. The resonant beam generated within the resonator acts as the carrier to transfer energy and information over the air. Thus, the narrow resonant beam can carry high power similar to the laser, and will cease immediately once a foreign object enters into the resonator, which enables high transmission power over long range with the premise of human safety [12].

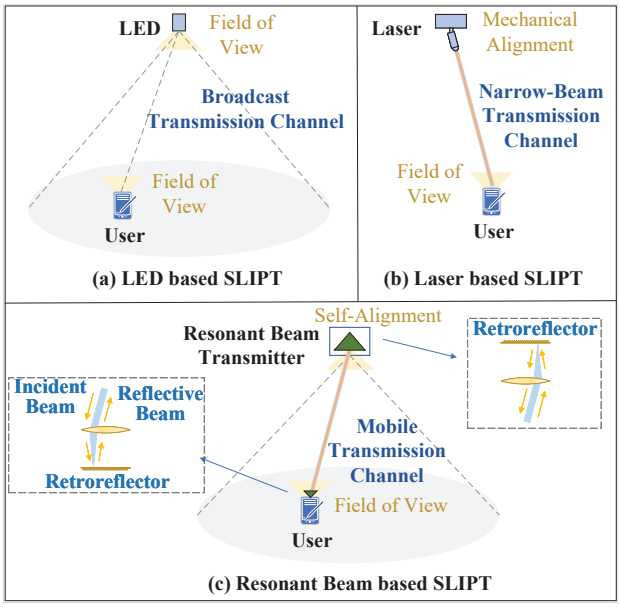

Fig. 1 Comparison of the resonant beam based SLIPT with the existing SLIPT schemes.

Moreover, two retroreflectors are adopted at both ends of the RBS. As in Fig. 1, retroreflectors can reflect the incident beam back parallel to the original direction regardless of the incident direction. RB-SLIPT with retroreflectors such as corner-cube reflector [13] and cat's eye [14] supports the capability of self-alignment. Therefore, receivers moving within the coverage of RB-SLIPT can be supplied with wireless energy and data through the mobile transmission channel. The mobility feature of RBS has been discussed in [9]. However, the model of the mobile transmission channel with self-alignment has not been established and the moving effects on energy/data transfer performance have not been analyzed. Thus, we build analytical models on the mobile transmission channel and propose a practical RB-SLIPT design, based on

Manuscript received September 20, 2020; revised March 5, 2021; accepted May 1, 2021. The work was supported by the National Key R&D Program of China under Grant 2020YFB2103900 and Grant 2020YFB2103902. It was also supported by the National Natural Science Foundation of China under Grant 61771344 and Grant 62071334. (*Corresponding author: Qingwen Liu.*) Mingqing Liu, Mingliang Xiong, and Qingwen Liu are with College of Electronics and Information Engineering, Tongji University, Shanghai 201804, China (e-mail: clare@tongji.edu.cn, xiongml@tongji.edu.cn, qliu@tongji.edu.cn). Shengli Zhou is with Department of Electrical and Computer Engineering, University of Connecticut, Connecticut, United States (e-mail: shengli.zhou@uconn.edu). Hao Deng is with the School of Software Engineering, Tongji University, Shanghai 201804, China (e-mail: denghao1984@tongji.edu.cn).

This article has been accepted for publication in a future issue of this journal, but has not been fully edited. Content may change prior to final publication. Citation information: DOI 10.1109/TWC.2021.3078808, IEEE Transactions on Wireless Communications

which the energy/data transfer performance under moving factors can be depicted.

Recently, many potential SLIPT schemes have emerged. The concept of SLIPT is at first proposed in an LED-based system with $1 \sim 2$mJ harvested energy, 25bit/second/Hz spectral efficiency, and $30^\circ \sim 50^\circ$ FOV with broadcast transmission channel [2]. For high-efficiency narrow-beam transfer, laser-based SLIPT is proposed to deliver 10.39mW charging power over 5.2m using 5 laser diode (LD) transmitters [8], with the comprise of mobility. As for the SLIPT receiver design, with the proposal of using a single PV for simultaneously data detection and energy harvesting providing 11.84Mb/s data rate and 30mW harvested power [15], laser-based SLIPT systems have made great advancements in state-of-the-art data rates from 0.5Gb/s [7] to 1Gb/s [16] with more than 40% energy conversion efficiency. Meanwhile, the capability of a single PV [3, 17] or a single photodiode (PD) [18, 19] for energy/data receiving in LED-based systems has been exploited sufficiently. However, to exploit the respective advantages as strong detection sensitivity and high energy conversion efficiency of the PD and the PV, an LED-based SLIPT scheme with a PD and a PV for data detection and energy harvesting respectively is proposed, with 0.1W harvested power and 15bits/sec/Hz achievable rate [4]. In summary, the existing SLIPT schemes have the conflict between high-efficiency transmission and mobile positioning of moving receivers, and the receiver design with both PV and PD is a potential way to obtain attractive performance for both energy and data transfer.

A resonant beam communication (RBCom) system with a single PV cell for simultaneous energy harvesting and data detection is proposed in [10]. Due to the energy-data transfer performance tradeoff of a single PV, the deliverable power of RBCom is below 50mW, which is not sufficient for powering mobile devices such as smartphones. Thus, the RB-SLIPT adopts the receiver design with a PV and an avalanche photodiode (APD) for energy and data receiving respectively. Moreover, the analytical models of the transmission channel in the above RBCom system don't support mobility analysis, which is one of the contributions of the current manuscript.

In this paper, we at first present the RB-SLIPT structure. After revealing the self-alignment mechanism with the transfer matrix method, we adopt the resonator mode analysis and laser output power calculation to depict the energy distribution in the mobile transmission channel. Then, we propose a practical RB-SLIPT design with a receiver adopting both PV and APD and evaluate the system performance. The RB-SLIPT can simultaneously provide more than 4W wireless charging power and 3Gb/s achievable data rate within the moving range of 3m distance and 20° FOV given 250W input power.

The contributions of this manuscript are:

1) We introduce a SLIPT system that can simultaneously realize safe energy-concentrated beam transfer and self-alignment without tracking control; meanwhile, simultaneous high deliverable charging power and high achievable data rate is achieved by using the PV and APD for energy harvesting and data receiving respectively.
2) We establish a mobile transmission channel model in RB-SLIPT, based on which the self-alignment mechanism of RB-SLIPT system is revealed and the energy distribution in the channel with a single transmitter is depicted.
3) We propose a practical design of simultaneous energy and information transfer using both PV and APD, based on which the performance of data/energy transfer with the impacts of moving factors can be quantitatively evaluated.

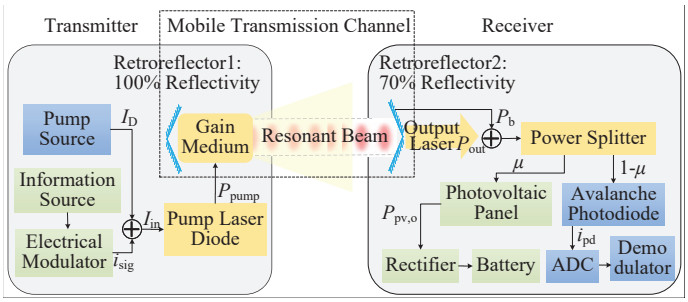

Fig. 2 Transceiver design of the resonant beam based simultaneous lightwave information and power transfer system.

The remainder of this paper is organized as follows. In Section II, we propose the RB-SLIPT design and describe its architecture and principle. In Section III, we build a mobile transmission channel model to prove the self-alignment and depict the energy distribution in the channel. Afterwards, we establish an analytical model of mobile energy and information transfer in RB-SLIPT in Section IV. In Section V, we demonstrate the channel factor, charging power, and achievable data rate of the proposed system through numerical analysis. Finally, we make a conclusion in Section VI.

II. System Overview

Figure 2 depicts the transceiver design of the RB-SLIPT system. The proposed system consists of the spatially separated transmitter and receiver, between which the mobile transmission channel is formed.

The transmitter contains a pump source, an information source, an electrical modulator, a pump LD, a gain medium, and a retroreflector1 (RR1) with 100% reflectivity. In the transmitter, an alternating-current (AC) current i_{sig} is generated from the information source and the electrical modulator, which is biased by a direct-current (DC) current I_{D} generated by the pump source. I_{in} containing I_{D} and i_{sig} drives the pump LD to generate the pump laser with power of P_{pump}. Then, the pump laser provides energy for the gain medium to stimulate light radiation carrying data and energy, similar to the RF amplifier. RR1 with 100% reflectivity is adopted to reflect the light from the receiver back towards the incident direction.

Fig. 3 (a) illustrates how the gain is achieved by using external pumping. In the gain medium, the number of particles in the lower energy level E_1 is greater than that in the higher energy level E_2. After pumped by the external pumping, the particles in E1 are loaded to E_2 to form the population inversion. Then, the stimulated radiation occurs to release photons realizing the light amplification. The pumping process in typical resonators, i.e., diode lasers, gas lasers, and solid-state lasers are illustrated in Fig. 3 (b), (c), and (d), with the specific structure using semiconductor materials, gas, and

This article has been accepted for publication in a future issue of this journal, but has not been fully edited. Content may change prior to final publication. Citation information: DOI 10.1109/TWC.2021.3078808, IEEE Transactions on Wireless Communications

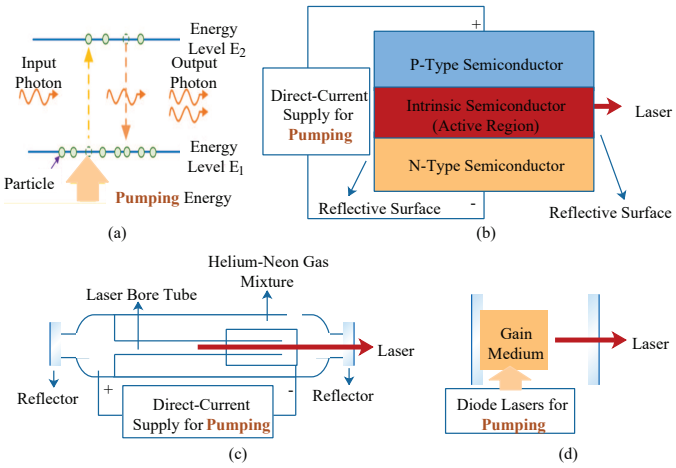

Fig. 3 Pumping principle (a) and process in typical lasers, i.e., (b) diode lasers, (c) gas lasers, and (d) solid-state lasers.

solid-state crystal as the gain medium, respectively. The RBS adopts the solid-state gain medium and the corresponding pumping method.

The receiver contains a retroreflector2 (RR2) with 70% reflectivity, a PV panel, an APD, and corresponding energy/data processing units. The output laser with power of P_{out} is output from the RR2 with 70% reflectivity. Then together with the background irradiance P_{b} caused by the ambient light, the output power enters a power splitter to be split into two streams with a specific ratio. One stream is sent to PV and converted to the charging current with $P_{\text{pv,o}}$. After being rectified, the power is ready for charging the battery. One stream is sent to APD, and a ratio of the input AC signal i_{sig} after transmission through the system is converted to the signal current i_{pd}. i_{pd} carrying information enters the demodulator for demodulation after passing the analog-to-digital converter (ADC).

The mobile transmission channel is formed by two retroreflectors and a gain medium. Similar to the traditional laser, the gain medium stimulates the light radiation, which can be reflected back and forth inside the resonant cavity and pass through the gain medium multiple times to be amplified. If the light power gain can compensate for the light power loss, the narrow laser outputs stably with high power. On the other hand, the mobile transmission channel is essentially an open-cavity, and the intra-cavity laser named as resonant beam is used to transfer energy/data over the air. Thus, with a resonant cavity that allows light to be retroreflected within it and sufficient input power, the resonant beam can be self-established between the transceivers. The two retroreflectors in the mobile transmission channel form a mobile resonant cavity (MRC). Due to the retro-reflective characteristics of the two retroreflectors, the resonant beam can be established within the MRC even as the two reflectors are not strictly facing each other, which guarantees the self-misalignment.

III. Mobile Transmission Channel Model

Mobile transmission channel of RB-SLIPT relies on the MRC to realize mobility. In this section, we investigate the MRC with two cat's eyes at both ends as a paradigm. We at

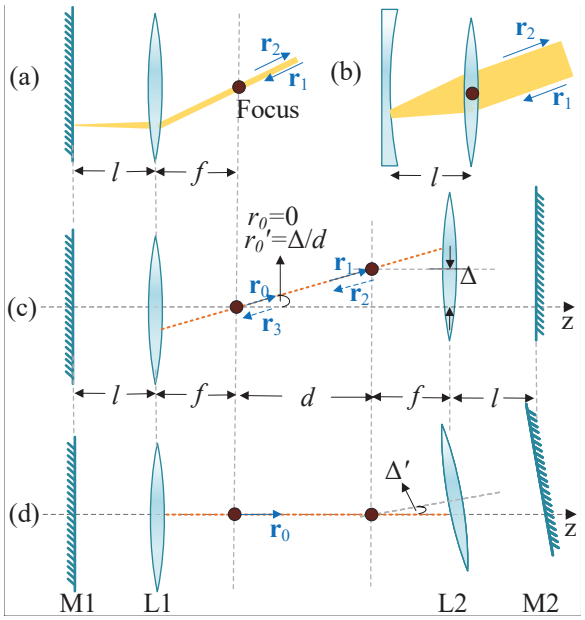

Fig. 4 Cat's eye structures and self-alignment of the mobile resonant cavity.

first prove the self-alignment characteristic of the MRC, after which we derive that the MRC with two deflected reflectors is equivalent to a Fabry-Perot (FP) resonator. Then, we adopt the laser mode analysis method and laser output principle to obtain the power output and depict the energy distribution in the mobile transmission channel.

A. Self-Alignment Mechanism of the Channel

We adopt the transfer matrix (i.e., ABCD matrix) method to define a round-trip transfer process of a ray inside the resonant cavity. Each component (including the free space) that a ray will pass through is described as a matrix with four elements, and passing through a serial of components is equivalent to the multiplication of each component's transfer matrix. As in Fig. 4(a), a cat's eye including a lens with focal distance f and a mirror with the interval between them l is described as $\mathbf{M}_{\text{cat}}$, and a ray represented by vector $\mathbf{r}_1$ after passing it is transferred to $\mathbf{r}_2$ as

$$\mathbf{r}_2 = \mathbf{M}_{\text{cat}}\mathbf{r}_1, \tag{1}$$

where $\mathbf{r}_1 = \begin{bmatrix} r_1 \\ r_1' \end{bmatrix}$. r_1 is the distance between the ray and optical axis, and r_1' is the slope of the ray about the optical axis. Then, $\mathbf{M}_{\text{cat}}$ is expressed as follows:

$$\begin{aligned}\mathbf{M}_{\text{cat}} = &\begin{bmatrix} 1 & f \\ 0 & 1 \end{bmatrix}\begin{bmatrix} 1 & 0 \\ -1/f & 1 \end{bmatrix}\begin{bmatrix} 1 & l \\ 0 & 1 \end{bmatrix}\begin{bmatrix} 1 & 0 \\ 0 & 1 \end{bmatrix} \\ &\begin{bmatrix} 1 & l \\ 0 & 1 \end{bmatrix}\begin{bmatrix} 1 & 0 \\ -1/f & 1 \end{bmatrix}\begin{bmatrix} 1 & f \\ 0 & 1 \end{bmatrix}.\end{aligned} \tag{2}$$

If $l = f$, $\mathbf{M}_{\text{cat}} = \begin{bmatrix} -1 & 0 \\ 0 & -1 \end{bmatrix}$. The cat's eye as in Fig. 4(b) includes a lens with focal length f and a curved mirror with

This article has been accepted for publication in a future issue of this journal, but has not been fully edited. Content may change prior to final publication. Citation information: DOI 10.1109/TWC.2021.3078808, IEEE Transactions on Wireless Communications

the radius of curvature ρ. Then the transfer matrix is

$$\mathbf{M}_{\mathrm{cat}'} = \begin{bmatrix} 1 & 0 \\ -1/f & 1 \end{bmatrix} \begin{bmatrix} 1 & l \\ 0 & 1 \end{bmatrix} \begin{bmatrix} 1 & 0 \\ -2/\rho & 1 \end{bmatrix} \begin{bmatrix} 1 & l \\ 0 & 1 \end{bmatrix} \begin{bmatrix} 1 & 0 \\ -1/f & 1 \end{bmatrix}. \tag{3}$$

If $l = f = \rho$, $\mathbf{M}_{\mathrm{cat}'} = \begin{bmatrix} -1 & 0 \\ 0 & -1 \end{bmatrix}$. Both the cat's eye structures in Fig. 4(a) and (b) have the capability of retroreflecting beams. However, beams being retroreflected by the cat's eye in Fig. 4(a) must pass through the focus of the lens (i.e., the pupil of the cat's eye), where a gain medium with limited size can be placed. Thus, we adopted the cat's eye in Fig. 4(a) with $l = f$. Moreover, it should be stated that the mentioned lenses above and below are thin lenses, and if the thick lens is considered, the thickness, index of refraction, and the distance between front face to principle plane of the thick lens are supposed to be added to the transfer matrix [20].

Then, a round-trip transfer matrix of a ray inside a resonant cavity is the multiplication of the matrices that a ray will pass through in a round trip, i.e., $\mathbf{M}_{\mathrm{tot}} = \mathbf{M}_1\mathbf{M}_2...\mathbf{M}_N$, where N is twice the number of components in the resonant cavity. Suppose a ray $\mathbf{r}_0$ can realize self-reproduction after a round-trip transfer, i.e.,

$$\mathbf{M}_{\mathrm{tot}}\mathbf{r}_0 = \mathbf{r}_0, \tag{4}$$

then $\mathbf{r}_0$ can be regarded as a vector representing the axis of the cavity. Rays parallel to the axis can be reflected back and forth inside the resonant cavity.

As in Fig. 4(c) and (d), the MRC of RB-SLIPT consists of two cat's eyes, where a cat's eye contains a mirror (M1/M2) and a lens (L1/L2) parallel to each other. z-axis which passes through the centers of L1 and M1 is defined as the origin optical axis of the MRC. Once the right-hand cat's eye consisting of L2 and M2 is off the z-axis, the MRC is defined as an off-axis system. In an off-axis system, the misalignment vector of the off-axis component is defined as

$$\mathbf{\Delta} = \begin{bmatrix} \Delta \\ \Delta' \end{bmatrix}, \tag{5}$$

where Δ is the distance between the element axis of off-axis component and origin optical axis, and Δ' is the slope of the element axis about the origin optical axis. Then, the relationship of $\mathbf{r}_1$ and $\mathbf{r}_2$ before and after passing through an off-axis component can be depicted as [20]

$$\mathbf{r}_2 = \mathbf{M}\mathbf{r}_1 + \mathbf{E}, \tag{6}$$

where $\mathbf{E}$ is an error vector expressed as

$$\mathbf{E} \equiv \begin{bmatrix} E \\ F \end{bmatrix} = [\mathbf{M}_\Delta - \mathbf{M}]\,\mathbf{\Delta}, \tag{7}$$

where $\mathbf{M}_\Delta$ represents the optical length difference matrix of the off-axis component. Thus, the transfer process of (6) can be depicted as an ABCDEF matrix [21]:

$$\begin{bmatrix} r_2 \\ r_2' \\ 1 \end{bmatrix} = \begin{bmatrix} A & B & E \\ C & D & F \\ 0 & 0 & 1 \end{bmatrix} \begin{bmatrix} r_1 \\ r_1' \\ 1 \end{bmatrix}. \tag{8}$$

In Fig. 4, suppose a ray $\mathbf{r}_0$ starts from the left focus of L1, $\mathbf{r}_0$ can be self-reproduced after a round-trip transfer process inside the MRC as

$$\mathbf{M}_{\mathrm{tot}}\mathbf{r}_0 + \mathbf{E}_{\mathrm{tot}} = \mathbf{r}_0, \tag{9}$$

then $\mathbf{r}_0$ represents the new optical axis of MRC after the moving of the right-hand cat's eye, where [21]

$$\mathbf{r}_0 = (\mathbf{I} - \mathbf{M}_{\mathrm{tot}})^{-1}\mathbf{E}_{\mathrm{tot}}. \tag{10}$$

To figure out $\mathbf{M}_{\mathrm{tot}}$ and $\mathbf{E}_{\mathrm{tot}}$, we expand (9) as follows:

$$\begin{aligned} \mathbf{r}_1 &= \mathbf{M}_{\mathrm{fs}}\mathbf{r}_0 \\ \mathbf{r}_2 &= \mathbf{M}_{\mathrm{cat}}\mathbf{r}_1 + \mathbf{E}_{\mathrm{M}} \\ \mathbf{r}_3 &= \mathbf{M}_{\mathrm{fs}}\mathbf{r}_2 \\ \mathbf{r}_0 &= \mathbf{M}_{\mathrm{cat}}\mathbf{r}_3 \end{aligned}, \tag{11}$$

Then, we have the following relationship [20]:

$$\begin{aligned} \mathbf{M}_{\mathrm{tot}} &= \mathbf{M}_{\mathrm{cat}}\mathbf{M}_{\mathrm{fs}}\mathbf{M}_{\mathrm{cat}}\mathbf{M}_{\mathrm{fs}} \\ \mathbf{E}_{\mathrm{tot}} &= \mathbf{M}_{\mathrm{cat}}\mathbf{M}_{\mathrm{fs}}\mathbf{E}_{\mathrm{M}} \end{aligned}. \tag{12}$$

$\mathbf{M}_{\mathrm{fs}} = \begin{bmatrix} 1 & d \\ 0 & 1 \end{bmatrix}$ denotes the transfer matrix over free space, where d is the distance between the two cat's eyes. $\mathbf{E}_{\mathrm{M}}$ is the error vector of the right-hand cat's eye after movement. As the case in Fig. 4(c), $\mathbf{\Delta} = \begin{bmatrix} \Delta \\ 0 \end{bmatrix}$. Thus, $\mathbf{E}_{\mathrm{M}}$ is given as following referring to (7):

$$\mathbf{E}_{\mathrm{M}} = \left(\begin{bmatrix} 1 & 4f \\ 0 & 1 \end{bmatrix} - \begin{bmatrix} -1 & 0 \\ 0 & -1 \end{bmatrix} \right) \begin{bmatrix} \Delta \\ 0 \end{bmatrix} = \begin{bmatrix} -2\Delta \\ 0 \end{bmatrix}. \tag{13}$$

Then, according to (10), we can obtain the elements of $\mathbf{r}_0$ as

$$\mathbf{r}_0 = \begin{bmatrix} 0 \\ \Delta/d \end{bmatrix}, \tag{14}$$

Similarly, if the right-hand cat's eye is slightly tilted about the x or y axis as in Fig. 4(b), the misalignment vector $\mathbf{\Delta} = \begin{bmatrix} 0 \\ \Delta' \end{bmatrix}$. With the above analysis on a round-trip transfer of a ray within the MRC, $\mathbf{r}_0$ is expressed as $\begin{bmatrix} 0 \\ 0 \end{bmatrix}$.

Evidently, $\mathbf{r}_0$ is coincident with the connection of the focuses of two cat's eyes, which represents the new optical axis of the MRC with one off-axis or tilted cat's eyes. Rays parallel to the new optical axis can be retroreflected inside the MRC rather than splitting over it. Thus, MRC with two cat's eyes is capable of realizing self-alignment with the new optical axis even if the two cat's eyes are not exactly facing each other due to the movement of the receiver.

As in Fig. 5, the line a2 passing through the focuses of both cat's eyes and the gain medium represents a ray reflected back and forth collinearly inside the MRC. Due to the off-axis of the right-hand cat's eyes, the angle between a2 and the normal vector of the cat's eye front face is θ. a1 is another ray which is generated by the gain medium and parallel to a2. Then, a1 is retroreflected by the right-hand cat's eye through points A, D, and C back towards the left-hand cat's eye along a3. Thus, there exists a resonant beam generated by and within

This article has been accepted for publication in a future issue of this journal, but has not been fully edited. Content may change prior to final publication. Citation information: DOI 10.1109/TWC.2021.3078808, IEEE Transactions on Wireless Communications

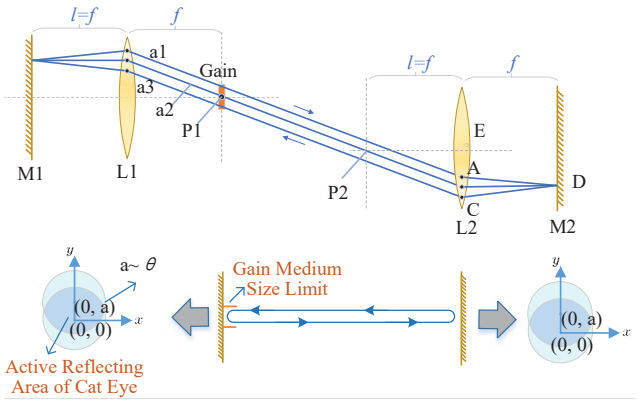

Fig. 5 Equivalent resonator for mobile resonant cavity.

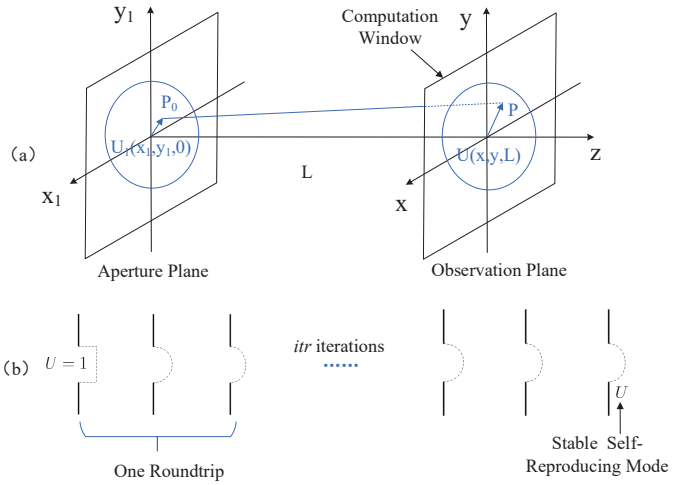

Fig. 6 Illustration of diffraction theory and self-reproducing mode calculation.

the size of the gain medium between the two cat's eyes, and the beam is symmetric about the new optical axis.

Moreover, according to the Fermat principle, the optical length of all rays inside the MRC is the same. Therefore, as the free space transmission distance is significantly larger than f, the MRC can be regarded as an FP resonator where the two end mirrors are located at the two focuses, and perpendicular to the new optical axis of the MRC.

B. Energy Distribution in the Channel

To find out the energy distribution of the mobile transmission channel, we should at first obtain the output laser power P_{out} in the receiver at any position within the system's FOV. As in Fig. 5, P1P2 is the optical axis of the MRC. We place a size-limited gain medium at the focus of the left-hand cat's eye, to generate the resonant beam inside the MRC with the excitation of the pump power P_{in}. M2 is partially transmissive so that a portion of resonant beam will pass through M2 to form the laser beam with power of P_{out}. Following the laser principle, the relationship between P_{in} and P_{out} is [22]

$$\begin{aligned} P_{\text{out}} =& A_b I_S \frac{(1-R)V_1}{1-RV_1V_2+\sqrt{RV_1V_2}\left[1/(V_SV_1)-V_S\right]}\times \\ & \left[\frac{\eta_{\text{excit}}P_{\text{in}}}{A_gI_S}-\left|\ln\left(\sqrt{RV_S^2V_1V_2}\right)\right|\right], \end{aligned} \tag{15}$$

where A_g, I_s, and V_s are the cross-sectional area, saturated light intensity, and loss factor caused by scattering and absorption of the gain medium, respectively; η_{excit} is the excitation efficiency and R is the reflectivity of M2; A_b is the overlapping area of resonant beam and gain medium and V_1, V_2 depict the loss factors caused by diffraction during single intra-cavity transmission, respectively. To accurately obtain P_{out}, we should calculate V_1, V_2, and A_b exactly. At first, we employ the resonator mode analysis method to calculate the eigenmode of the MRC.

The active reflecting area of the cat's eye is affected by the incident angle θ of the beam. We adopt the indication function to depict the reflective area by 1 and the non-reflective area by 0. Then as in Fig. 5, the active reflecting area of the left-hand and right-hand cat's eye can be depicted as

$$T_1(x,y;r,\theta)=\begin{cases} 1, x^2+y^2\le r^2, y\ge a/2 \\ \text{ and } x^2+(y-a)^2\le r^2, y\le a/2 \\ 0, \text{ else} \end{cases}, \tag{16}$$

where $a=2f\tan\theta$, and r is the radius of L1, L2, M1, and M2. Moreover, the size-limited gain medium limits the active reflecting area of the left-hand cat's eye, which is depicted as

$$T_2(x,y;r_g,\theta)=\begin{cases} 1, x^2+y^2\le (r_g\cos\theta)^2 \\ 0, \text{ else} \end{cases}, \tag{17}$$

where r_g is the radius of the gain medium surface.

For the equivalent FP resonator in Fig. 5, the active reflecting area of the left-hand mirror is $T_l = T_1 \cdot T_2$, and $T_r = T_1$ for the right-hand mirror. Based on the above proof and inferences, we can calculate the modes of the FP resonator as of the MRC using diffraction theories.

As in Fig. 6(a), if the light field distribution on one of the cavity mirror is known, one can obtain the amplitude and phase distribution of light field at any position in the cavity [23]. The light field at $Z=0$ can be regarded as a set of secondary waves. Thus, after the over-the-air transmission of the light field, the coherent superposition of the secondary waves of all secondary waves on the wavefront at each point on $Z=L$ constitutes the vibration of each point, forming a new light field distribution. The above process can be depicted as the Fresnel-Kirchhoff diffraction integral formula as

$$\begin{aligned} U(x,y,L)=&\frac{\exp(jkL)}{j\lambda L}\iint_T U(x_1,y_1,0)\times \\ & \exp\left\{j\frac{\mathrm{k}}{2L}\left[(x-x_1)^2+(y-y_1)^2\right]\right\}\mathrm{d}x_1\mathrm{d}y_1, \end{aligned} \tag{18}$$

where $j:=\sqrt{-1}$, L is the resonator length, $k=2\pi/\lambda$ is the wave number, and λ is the wavelength of resonant beam. Suppose $U(x_1,y_1,0)$ represents the field on the left-hand mirror of the FP resonator, then $U(x,y,L)$ is the field

This article has been accepted for publication in a future issue of this journal, but has not been fully edited. Content may change prior to final publication. Citation information: DOI 10.1109/TWC.2021.3078808, IEEE Transactions on Wireless Communications

on the other mirror and T is the active reflecting area of the left-hand mirror.

For high-speed numerical calculation, Fast-Fourier-Transform (FFT) is adopted to find numerical solution of diffraction process [24]. Equation (18) can be rewritten as the following convolution form:

$$U(x,y,L)=\iint_T U\left(x_1,y_1,0\right)h\left(x-x_1,y-y_1\right)\mathrm{d}x_1\mathrm{d}y_1, \tag{19}$$

where $h\left(x-x_1,y-y_1\right)$ named as impulse response can be expressed as

$$h(x,y)=\frac{\exp(jkL)}{j\lambda z}\exp\left[\frac{jk}{2L}\left(x^2+y^2\right)\right], \tag{20}$$

then the formula can be rewritten as [24]

$$\mathscr{F}\{U(x,y,z)\}=\mathscr{F}\{U(x_1,y_1,0)\}\cdot\mathscr{F}\{h(x,y)\}, \tag{21}$$

where $\mathscr{F}$ denotes the Fourier transform. Moreover, the fields before and after passing through the cat's eye's front face $U^-(x,y)$ and $U(x,y)$ have the following relationship [25]:

$$U(x,y)=T(x,y)\cdot U^-(x,y), \tag{22}$$

where $T(x,y)$ represents the active reflecting area of the cat's eye. Thus, the self-consistent integral formula for one round-trip field transmission is

$$\begin{aligned}U(x,y,L)=&\mathscr{F}^{-1}\{\mathscr{F}\{\mathscr{F}^{-1}\{\mathscr{F}\{U(x,y,L)\cdot T_r(x,y)\}\cdot\\&\mathscr{F}\{h(x_1,y_1)\}\}\cdot T_l(x_1,y_1)\}\cdot\mathscr{F}\{h(x,y)\}\}\cdot\\&T_r(x,y),\end{aligned} \tag{23}$$

where $\mathscr{F}^{-1}$ denotes the inverse Fourier transform process.

Based on the Fox-Li method [26], we are supposed to iterate (23) t times to calculate the eigenmode of the resonator. As in Fig. 6(b), the light field oscillating back and forth in the cavity can be equivalent to the light field continuously passing through a series of apertures and finally forming a stable light field distribution. Suppose the original light field distribution $U(x,y,L)=1$, which represents a uniform beam profile, the light field on the output plane is gradually stable during iterations [13, 25, 26]. Eventually, the forms of field distribution $U_t(x,y,L)$ after t iterations and $U_{t-1}(x,y,L)$ after $t-1$ iterations are exactly identical, except for the constant factor difference on amplitude and phase. Then $U_t(x,y,L)$ can be regarded as the self-reproducing mode, or namely the eigenmode of the stable resonator.

For simplicity, we assume only the fundamental mode, whose shape is similar to the Gaussian beam profile, reserves in the resonator after Fox-Li iterations [26]. Then, we can find the beam spot size A_s using the method for determining Gaussian beam radius [27] with $U_t(x,y,0)$, and the loss factor of the one-way transmission as

$$V_1=\frac{|U_t(x,y,L)|^2}{|U_t(x,y,0)|^2},\quad V_2=\frac{|U_t(x,y,0)|^2}{|U_t(x,y,L)|^2}. \tag{24}$$

Finally, we can obtain the receiver's output laser power P_{out} with respect to the input power P_{in}, the distance L between the two cat's eyes, and the translation angle θ of the remote cat's eye. Figure 7 depicts the power distribution on the receiving plane when the input power is 150W and the receiving plane is 3m and 2m away from the transmitter.

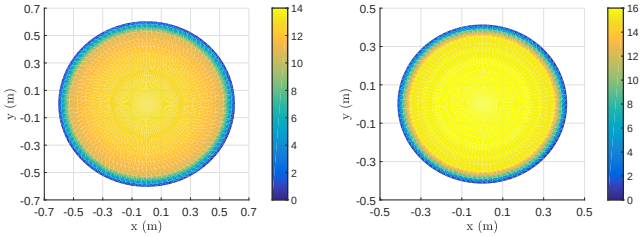

(a) (b)

Fig. 7 Optical power distribution (output laser power P_{out} in the receiver) with the input power $P_{\text{in}}=150W$. The height of the transmitter is (a) 3 m; (b) 2 m.

IV. Energy and Data Flow in an Exemplary RB-SLIPT System

In this section, we present a practical RB-SLIPT system design embedding a PV panel for energy harvesting and an APD for data receiving respectively at the receiver. We will detail the energy and data transfer flow of RB-SLIPT from three aspects: signal generating and power input at the transmitter, path loss in the mobile transmission channel, and energy/data processing at the receiver.

A. Signal Generating and Power Input at the Transmitter

1) Signal Generating: We adopt the optical orthogonal frequency division multiplexing (OFDM) method for signal modulation [28]. For indoor light communication applications, the narrow-band interference generated by artificial light sources will affect the performance of single carrier modulation schemes such as pulse width modulation (PWM) and pulse amplitude modulation (PAM) [29, 30]. However, OFDM technology can effectively solve the problems of inter-symbol interference and narrow-band interference caused by optical signal diffusion [16, 17].

At the transmitter, let s denote an input bitstream and s is at first mapped to the discrete modulation symbols, i.e., $s_1\ s_2\ \cdots\ s_{N/2-1}$, where N is the number of subcarriers. Then, the Hermitian symmetry is imposed on the data vector as $\mathbf{S}=\left[0\ s_1\ s_2\ \ldots\ s_{N/2-1}\ 0\ s^*_{N/2-1}\ \cdots\ s^*_2\ s^*_1\right]$ so that the output of the inverse discrete Fourier transform (IDFT) block can be real [31]. As illustrated in Fig. 2, we denote $i_{\text{sig}}(t)$ as a source signal from the electrical modulator; then $i_{\text{sig}}(t)$ after the IDFT operation and adding DC-bias can be presented as

$$i_{\text{sig}}(t)=\sum_{k=0}^{N-1}\underbrace{\frac{1}{\sqrt{N}}S(k)e^{j\frac{2\pi k}{N}t}}_{i_{\text{sig},k}(t)},t=0,1,\ldots,N-1, \tag{25}$$

where $i_{\text{sig},k}(t)$ represents the signal on k_{th} subcarrier, and $S(k)$ is the corresponding element of $\mathbf{S}$.

This article has been accepted for publication in a future issue of this journal, but has not been fully edited. Content may change prior to final publication. Citation information: DOI 10.1109/TWC.2021.3078808, IEEE Transactions on Wireless Communications

Then, a DC component from the pump source acts as a DC offset to the source signal. Thus, the generated signal at the transmitter can be given as

$$I_{\text{in}}(t) = I_{\text{D}} + i_{\text{sig}}(t), \tag{26}$$

where I_{D} is the DC offset and i_{sig} is an AC component carrying the data that needs to be sent out.

2) Power Input: For a thin-disk solid laser, an LD is adopted to pump the thin-disk gain medium. The electric current I_{in} at first drives the LD to generate the pump laser with power P_{pump} with the relationship as [32]

$$P_{\text{pump}} = \frac{hc_0}{q\lambda_{\text{e}}}\eta_e\left(I_{\text{in}} - I_{\text{th}}\right) \tag{27}$$

where $h = 6.62607015 \times 10^{-34}\text{J}\cdot\text{s}$, $c_0 = 3 \times 10^8\text{m/s}$, $q = 1.6\times10^{-19}\text{C}$, $\lambda_{\text{e}} = 808\text{nm}$ are the Plancks constant, the speed of light, the electron charge, and the emission light wavelength, respectively; η_e is the external quantum efficiency which is the multiplication of carrier injection efficiency and photon extraction efficiency; I_{th} is a temperature-dependent constant threshold current. I_{D} contributes to the input current exceeding the LD's threshold current I_{th}.

Then, the pump power is absorbed by the gain medium and converted to the power stored in the upper laser level inside the gain medium P_{avail} with efficiency η_a as

$$\begin{aligned} P_{\text{avail}} &= \eta_a P_{\text{pump}} \\ &= \eta_{\text{excit}} P_{\text{in}}, \end{aligned} \tag{28}$$

where $\eta_{\text{excit}} = \eta_{\text{a}}\eta_P$ represents the excitation efficiency. P_{in} denotes the input power containing both the AC and DC signal to the laser diode, and η_P is defined as the pump efficiency. Thus, P_{avail} is available for generating the resonant beam, which can be regarded as the power of the transmitted signal.

B. Path Loss in the Mobile Transmission Channel

For traditional SLIPT systems, the path loss of the transmission channel is caused by the beam divergence and misalignment of the transmitter and receiver. For the RB-SLIPT system, the resonant beam power which carries information and energy will increase as passing through the gain medium, and decrease as experiencing the diffraction losses, losses inside the medium, and output coupling. Due to the characteristics of long-range intra-cavity transfer and self-alignment, the intra-cavity diffraction loss cannot be neglected in the mobile transmission channel. As in Sec III, we can obtain the diffraction loss of one-way transmission inside the MRC as (24). Thus, the diffraction loss factor η_{diff} can be depicted as

$$\eta_{\text{diff}} = \sqrt{V_1 V_2}. \tag{29}$$

In the RB-SLIPT system, the transmission channel is essentially a separated resonant cavity, and the resonant beam carrying energy and data within the cavity inherits the features of lasers, i.e., monochromaticity, directionality, and coherence. Thus, the resonant beam transmission loss over the air within several meters is negligible. However, as the resonant beam transfers within the cavity, the diffraction loss that occurs as the beam passes through the optical devices such as lenses cannot be neglected, as the long transmission distance will lead to larger beam divergence, causing larger diffraction loss. Thus, the diffraction loss is dominant to the path loss during long-range transmission. From Section III, the diffraction loss in the mobile transmission channel relies on the size of system components, the distance, and the deflection angle between the transmitter and receiver.

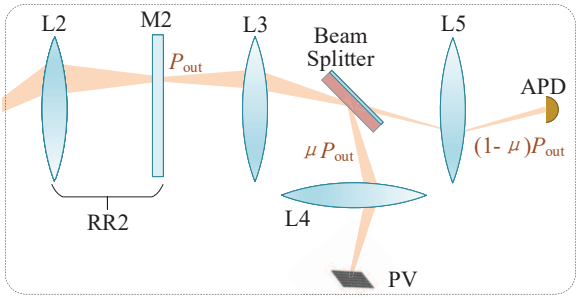

Fig. 8 RB-SLIPT receiver design with a power splitter.

C. Energy/Data Processing at the Receiver

Similar to the traditional laser system, the output laser power P_{out} will be extracted from P_{avail} after experiencing the path loss during the channel transmission, internal loss of the gain medium, and the loss due to the output coupling, where the extraction efficiency can be depicted as [22]

$$\eta_{\text{extr}} = \frac{\eta_b(1-R)V_1}{1-\eta_{\text{diff}}^2 R + \eta_{\text{diff}}\sqrt{R}\left[1/(V_S V_1) - V_S\right]}, \tag{30}$$

with $\eta_b = A_b/A_g$ denoting the overlap efficiency of the gain medium.

Then, the output laser power can be presented from (15), (28), (29), and (30) as

$$P_{\text{out}} = \eta_{\text{extr}}\eta_{\text{excit}} P_{\text{in}} - c, \tag{31}$$

where $c = \eta_{\text{extr}} A_g I_s \left|\ln\left(\eta_{\text{diff}} V_S \sqrt{R}\right)\right|$ represents the threshold of the laser output in the RB-SLIPT system. The parameter η_{extr} contains the impacts of various losses in the system, and η_{excit} depicts the stimulation process of the thin-disk gain medium. Then, the output laser power is spilt into two streams to be received by the PV and APD, respectively.

Figure 8 shows an exemplary RB-SLIPT receiver design with a power splitter. Here we adopt a beam splitter to split power and determine the split ratio $0 \le \mu \le 1$ through coating methods. μ is the reflectance of the beam splitter and $1-\mu$ is the transmittance. Thus, μP_{out} is received by a PV panel for energy harvesting and $(1-\mu)P_{\text{out}}$ is collected by an APD for information detection. Lens L3, L4, and L5 are adopted to focus the beam onto devices, i.e., beam splitter, APD, and PV, and the above devices are placed at the focuses of the lenses. Thus, beams can impinge on the PV/APD even in movement.

1) Energy Harvesting: Figure 9 depicts the equivalent circuit of PV for energy harvesting. PV under illumination can be regarded as a constant current source in parallel with diode. I_{ph} represents the photo-generated current, and I_{d} denotes the current that is used to counteract the junction current of p-n junction. The additional resistance due to PV's material

This article has been accepted for publication in a future issue of this journal, but has not been fully edited. Content may change prior to final publication. Citation information: DOI 10.1109/TWC.2021.3078808, IEEE Transactions on Wireless Communications

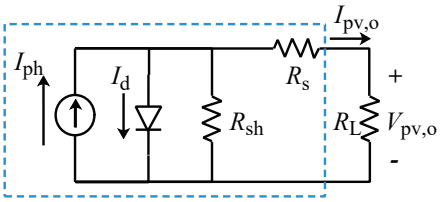

Fig. 9 DC equivalent circuit of PV for energy harvesting [8].

properties is represented by series resistance R_{s} and the edge leakage is modeled by a parallel shunt resistance R_{sh}. Finally, R_{L} represents the load, i.e., battery to be charged, with the PV's output current $I_{\text{pv,o}}$ and output voltage $V_{\text{pv,o}}$.

Then according to Kirchhoff's law, the current-voltage (I-V) characteristics of a PV panel at a maximum power point can be described as

$$I_{\text{pv,o}} = I_{\text{ph}} - I_{\text{d}} - \frac{V_{\text{d}}}{R_{\text{sh}}}, \tag{32}$$

where V_{d} is the voltage across the diode follows

$$V_{\text{d}} = V_{\text{pv,o}} + I_{\text{pv,o}} R_{\text{s}}. \tag{33}$$

Moreover, the current I_{d} through the diode is

$$I_{\text{d}} = I_0 \left(\mathrm{e}^{c_1 V_{\text{d}}} - 1\right), \tag{34}$$

where I_0 is the reverse saturation current, $c_1 = 1/n_{\text{s}} n V_T$ is the PV panel factor, with n_{s} the number of cells connected inside a PV panel, n the diode ideality factor, and $V_T = (kT)/q$ is the thermal voltage of the diode, with k the Boltzmann's constant and T the temperature in Kelvin.

Moreover, I_{ph} depends on the light power received by the PV panel $P_{\text{pv,i}}$. Assume the output laser power for energy harvesting is 100% harvested by the PV, i.e., $P_{\text{pv,i}} = \mu P_{\text{out}}$, the relationship between photocurrent I_{ph} and PV's input laser power $P_{\text{pv,i}}$ can be depicted as

$$\begin{aligned} I_{\text{ph}} &= \rho_1 P_{\text{pv,i}} \\ &= \mu \rho_1 (\eta_{\text{extr}} \eta_{\text{excit}} P_{\text{in}} - c), \end{aligned} \tag{35}$$

where ρ_1 is the conversion responsivity factor which depicts the optical-to-electrical conversion efficiency and can be measured in A/W. From (32), (33), and (35), we can obtain the output power $P_{\text{pv,o}}$ of the PV panel available for charging the battery as

$$P_{\text{pv,o}} = I_{\text{pv,o}} V_{\text{pv,o}}. \tag{36}$$

Then, the end-to-end DC power efficiency η_{sys} of the RB-SLIPT system can be calculated as

$$\eta_{\text{sys}} = \frac{P_{\text{pv,o}}}{P_{\text{in}}}. \tag{37}$$

2) Data Receiving: A portion of the laser beam is received by the APD and converted to the output signal current:

$$P_{\text{pd}} = (1-\mu) P_{\text{out}}, \tag{38}$$

At the receiver part, the following three aspects are detailed for the communication performance analysis.

- Received Signal: To present the signal gain in the mobile transmission channel of the RB-SLIPT, we can rewrite (38) as follows according to (27), (28), and (31):

$$\begin{aligned} i_{\text{pd}} &= \rho_2 P_{\text{pd}} \\ &= \rho_2 (1-\mu) \left[\gamma \left(I_{\text{in}} - I_{\text{th}}\right) - c\right], \end{aligned} \tag{39}$$

where ρ_2 represents the optical-to-electrical conversion responsivity of APD expressed as [33, 34]

$$\rho_2 = \frac{q \lambda \eta_e}{hc} M, \tag{40}$$

where M is the multiplication factor of the transimpedance amplifier inside the APD relying on the temperature and bias voltage. Then, γ is presented as

$$\gamma = \eta_{\text{extr}} \eta_{\text{a}} \eta_e \frac{hc}{q \lambda_{\text{e}}}. \tag{41}$$

γ and c are constants at given transmission distance and deflection angle between the transceiver, which illustrates the linear modulation ability of mobile transmission channel for communication. Then, γ is modeled as the channel gain for signal transfer in RB-SLIPT, which reflects the channel condition depending on the transmission distances and deflection angles. Thus, the time domain signal on k_{th} subcarrier received by the user can be described as [35]

$$i_{\text{pd},k}(t) = \rho_2 (1-\mu) \gamma i_{\text{sig},k}(t) + n_k(t), \tag{42}$$

where $n_k(t)$ is the noise signal on the k_{th} subcarrier.

- Noise Analysis: We analyze the shot noise generated through the optical-to-electrical conversion in the APD and the thermal noise caused by the resistors in the APD system. The variance of the noise signal with zero mean on k_{th} subcarrier can be expressed as [31]

$$\sigma_k^2 = N_{\text{total}} W / N, \tag{43}$$

where W is the modulation bandwidth. The noise signal can be modeled as additive white Gaussian noise with power spectral density (PSD) profile denoted as N_{total}, which is the sum of laser intensity noise, shot noise, and thermal noise:

$$N_{\text{total}} = N_{\text{L}} + N_{\text{sh}} + N_{\text{th}}. \tag{44}$$

Laser intensity noise primarily comes from spontaneous light emissions, which is depicted as [36]

$$N_{\text{L}} = S_{\text{RIN}} P_{\text{pd}}, \tag{45}$$

where S_{RIN} is the relative intensity noise (RIN) of the laser. The one-side PSD of the shot noise in A^2/Hz can be expressed as [10]

$$N_{\text{sh}} = 2q\rho_2 (P_{\text{pd}} + P_{\text{b}} + P_{\text{det}}) M F, \tag{46}$$

where F is the excess-noise factor for the APD derived from the effective ionization coefficient k_{eff} as [33]

$$F = M k_{\text{eff}} + (1 - k_{\text{eff}}) \left(2 - \frac{1}{M}\right). \tag{47}$$

$P_{\rm b}$ is the background power caused by the ambient light (sunlight or LED light), which is expressed as [33]

$$P_{\rm b} = \eta_{\rm Rx} H_{\rm b} B_{\rm IF} A_{\rm Rx} \Phi_{\rm Rx} R, \tag{48}$$

where $\eta_{\rm Rx} = 0.5$ is the optical efficiency of the signal receiving unit, $H_{\rm b} = 0.2{\rm Wnm^{-1}sr^{-1}m^{-2}}$ represents the background spectral radiance, $B_{\rm IF} = 20{\rm nm}$ is the optical bandwidth of the filter installed behind the output coupler RR2; $A_{\rm Rx} = 4.52{\rm cm}^2$, $\Phi_{\rm Rx} = 0.7041{\rm sr}$, and $R = 0.7$ are the receiving area, solid angle, and transmittance of RR2, respectively. Thus, the $P_{\rm b}$ is estimated as 9.56×10^{-6}W. $P_{\rm det}$ is the detector noise power formulated as [33]

$$P_{\rm det} = \sqrt{W} N_{\rm det}, \tag{49}$$

where $B_{\rm det}$ is the detector bandwidth and $N_{\rm det}$ is the noise equivalent power (NEP).

The thermal noise is generated by the load resistor $R_{\rm L,pd}$, of which the one-side PSD can be described as [36, 37]

$$N_{\rm th} = 4kTF/R_{\rm L,pd}. \tag{50}$$

- Signal-to-Noise Ratio (SNR): To evaluate the performance of the communication in the RB-SLIPT system, we analyze the SNR of the channel. We depict the channel performance from the SNR of each subchannel, and the SNR of the k_{th} sub-channel regardless of each subchannel's frequency selectivity is expressed as [31]

$$\mathrm{SNR}_k = \frac{\left[\rho_2 (1-\mu)\gamma i_{{\rm sig},k}\right]^2}{\sigma_k^2}. \tag{51}$$

We adopt the M-array quadrature amplitude modulation (M-QAM) method and the OFDM signal is clipped on both sides of the time-domain distribution with the clipping levels at -3.2ε and 3.2ε [38], where $\varepsilon = \rho_2 P_{\rm pd}/2$ considering the average received optical signal power. Thus, the upper part of the above equation (51) can be expressed as $(\rho_2 P_{\rm pd}/2/3.2)^2/(N-2)$. It should be stated that ρ_2 and σ_k^2 depend on the key factors of APD, i.e., multiplication factor M and excess-noise factor F.

Then, in OFDM systems with the M-QAM method, the average spectral efficiency is [17]

$$\eta_{\rm sp} = \frac{\sum_{k=1}^{N/2-1} \log_2 M_k}{(N + N_{\rm cp})(1+\beta)}, \tag{52}$$

where N is the FFT size which is equal to the number of subcarriers, β is the roll-off factor of the filter, $N_{\rm cp}$ is the OFDM cyclic prefix length, and M_k is the size of the M-QAM array constellation on subcarrier k. Then the data rate is obtained as [38]

$$R_{\rm b} = 2\eta_{\rm sp} W. \tag{53}$$

The theoretical bit error rate (BER) of M-QAM is then expressed as [17]

$$\mathrm{BER} \approx \frac{4}{\log_2 M_k}\left(1 - \frac{1}{\sqrt{M_k}}\right) \times \sum_{i=1}^{2}\sum_{k=1}^{N} Q\left((2i-1)\sqrt{\frac{3\mathrm{SNR}_k \log_2 M_k}{4\eta_{sp}(M_k-1)}}\right), \tag{54}$$

where $Q(\cdot)$ is the complementary cumulative distribution function (CCDF) for the standard normal distribution.

After comparing with the capacity calculation of a channel model for the free-space optical communication [39–41], we adopt the following formula to depict the achievable data rate of the RB-SLIPT system as [31]

$$R_{\rm a} = \sum_{k=1}^{N/2-1} (W/N) \log_2 (1 + \mathrm{SNR}_k). \tag{55}$$

V. Numerical Results and Discussion

In this section, we numerically analyze the channel factor and the energy/data transfer capability of the RB-SLIPT system. As for the mobility-enhanced system, we will specifically analyze the impacts of the moving range (i.e., transmission distance and deflection angle), the DC offset power, and the split ratio on the performance of the proposed system.

A. Parameters

TABLE I Parameter of Resonant Beam System [22]

Parameter	Symbol	Value
Cat's eye radius	r	12mm
Gain medium radius	r_g	3mm
Resonant beam wavelength	λ	1.064×10^{-6}m
Output coupler reflectivity	R	0.7
Medium saturated intensity	I_s	1.26×10^7W/m^2
Loss factor in medium	V_s	0.99
Excitation efficiency	$\eta_{\rm excit}$	0.5148 [42]
Gain stored efficiency	$\eta_{\rm a}$	0.72
External quantum efficiency	η_e	0.9 [10]

TABLE II Parameter of Energy/Data Transfer [33, 43]

Parameter	Symbol	Value
PV conversion responsivity	ρ_1	0.0161A/W
Reverse saturation current	I_0	9.89×10^{-9}A
Diode ideality factor	n	1.105
Number of serial PV cells	$n_{\rm s}$	40
Series resistance	$R_{\rm s}$	0.93Ω
Shunt resistance	$R_{\rm sh}$	52.6kΩ
PV load resistor	$R_{\rm L}$	100Ω
Temperature in Kelvin	T	298.15K
APD gain	M	135
Effective ionization coefficient	$k_{\rm eff}$	0.005
Detector bandwidth	W	422MHz
Detector NEP	$N_{\rm det}$	0.19pW/Hz$^{1/2}$
Relative intensity noise	$S_{\rm RIN}$	−130dB/Hz [36]
APD load resistor	$R_{\rm L,pd}$	10KΩ [37]

TABLE III Parameter of Fox-Li and FFT algorithm [24, 26]

Parameter	Symbol	Value
FoxLi iteration number	t	300
Sampling number	S_N	2048
Computation window expand factor	G	2

The parameters of the gain medium are from an example of a diode-end-pumped Nd:YVO_4 laser in [22, 42]. The thin-disk Nd:YVO_4 gain medium is with high excitation efficiency

This article has been accepted for publication in a future issue of this journal, but has not been fully edited. Content may change prior to final publication. Citation information: DOI 10.1109/TWC.2021.3078808, IEEE Transactions on Wireless Communications

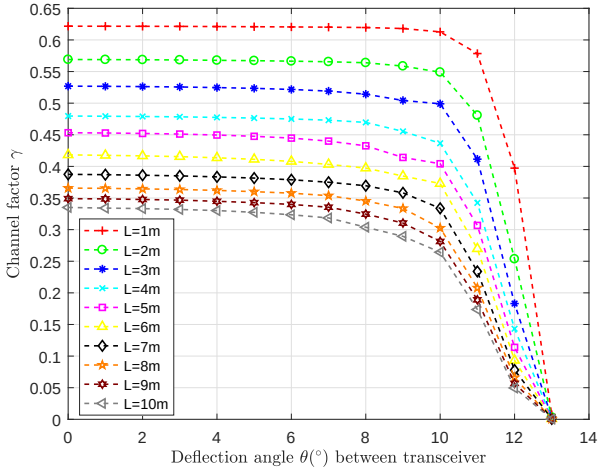

Fig. 10 Channel factors γ of the RB-SLIPT with different transmission distances L and deflection angles θ.

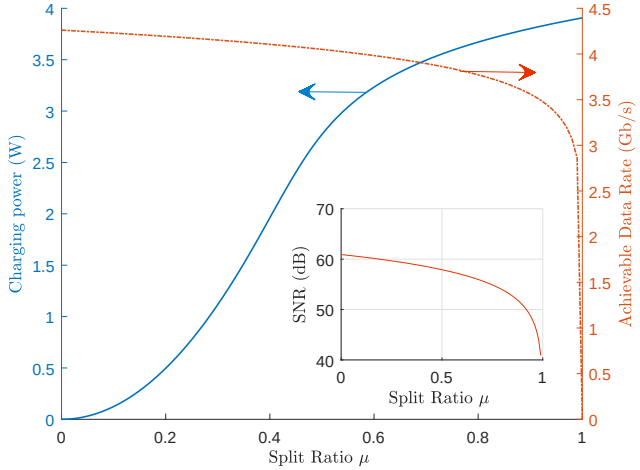

Fig. 11 Charging power and achievable data rate as a function of deflection angle θ with different split ratio μ under transmission distance $L = 3$m.

and the thin-disk structure enables a larger FOV of the RB-SLIPT transmitter. The 808nm diode laser is chosen to pump the gain medium and the infrared beam with the wavelength of 1064nm is stimulated as the resonant beam. Then, we adopt a vertical multi-junction PV cell for energy harvesting and obtain the parameters for the PV's equivalent circuit through fitting operations using the measured data in [43, 44]. Moreover, parameters of APD for data receiving are from [33].

For the FFT numerical calculation, the calculation plane and the impulse response function need to be sampled first, and the sampling number S_N is generally a power of 2. Moreover, zero-padding is needed to avoid aliasing effects as in Fig. 6. The computation window length $2Gr$ is defined as the length of zero-padded aperture, where G is the computation window expand factor, and r is the front face radius of the cat's eye. Appropriate value selection of S_N and G can avoid the aliasing effects and simulate the resonant beam transmission accurately for the FFT process, and the rules are referred to [24]. Moreover, according to the calculations in [26], we choose the number of iterations before the termination of the iterative process. We specify the RBS parameters, energy and data transfer parameters, and FFT and Fox-Li algorithm parameters in Table I, II, and III, respectively.

B. Channel Factor of the Mobile Transmission Channel

In this paper, we have proposed an analytical model for the energy distribution analysis of the mobile transmission channel, so that we are capable of modeling the channel accurately as a function of mobility factors such as transmission distance, i.e., cavity length L, and the deflection angle between transceiver θ. Figure 10 depicts the channel factors γ of the proposed system with varying L and θ. γ doesn't change obviously as the deflection angle between the transceiver is below 10°. However, as the angle is larger than 10°, γ declines sharply and turns to 0 with $\theta = 13^\circ$. The maximum allowable angle depends on the parameters (i.e., focus length and front face radius) of the cat's eye. Moreover, as the transmission distance L changes from 1m to 10m, γ decreases correspondingly. The increment of the cavity length leads to larger beam divergence, thus the diffraction loss during resonant beam transmission grows and the channel factor decreases. The diffraction loss is obtained accurately through numerical methods introduced in Section III.B, which is not linearly dependent on the cavity length.

C. Energy-Data Transfer Performance of RB-SLIPT

At the receiver, the output laser beam at first enters into a power splitter and is split into two streams with ratio μ for energy and data harvesting, respectively. To ensure that the incident optical power onto the APD is below the APD's saturated power, we place an attenuator with 1% transmittance above the APD. Thus, as in Fig. 11, we analyze how the split ratio impacts the energy/data transfer performance given an input power 200W. We can find as μ grows, the charging power improves significantly, while the degradation trend in data transfer performance is slow until μ approaches 1. To enhance clarity, we plot the average SNR as a function of μ, where SNR reduces as the μ increases similar to the downward trend of achievable data rate. The value of μ determines the energy/data transfer performance and the improvement of charging power is more obvious. Thus, in the following analysis, we choose the split ratio $\mu = 0.99$ for maximizing the energy/data transfer capability. It should be stated that we set subcarrier number $N = 1024$ in the analysis above and below.

Figure 12 shows the charging power and achievable data rate as a function of input power of the DC offset I_{D}, with transmission distance $L = 2$m and 3m as well as deflection angle $\theta = 0^\circ$ and 10°. As the input power increases, the charging power from PV grows over 4W and the communication performance improves correspondingly from 2.6Gb/s to 3.1Gb/s. With the increase of input power, the output laser power increases linearly, while the growth rate of the charging power gradually slows down. That's because

This article has been accepted for publication in a future issue of this journal, but has not been fully edited. Content may change prior to final publication. Citation information: DOI 10.1109/TWC.2021.3078808, IEEE Transactions on Wireless Communications

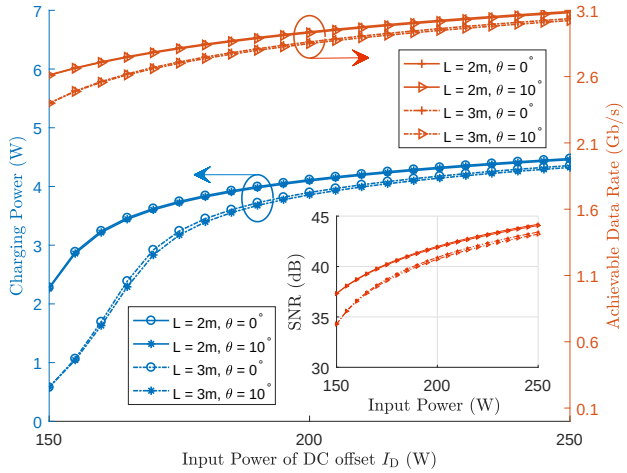

Fig. 12 Charging power and achievable data rate as a function of input power of the DC offset I_{D} with different transmission distances and deflection angles.

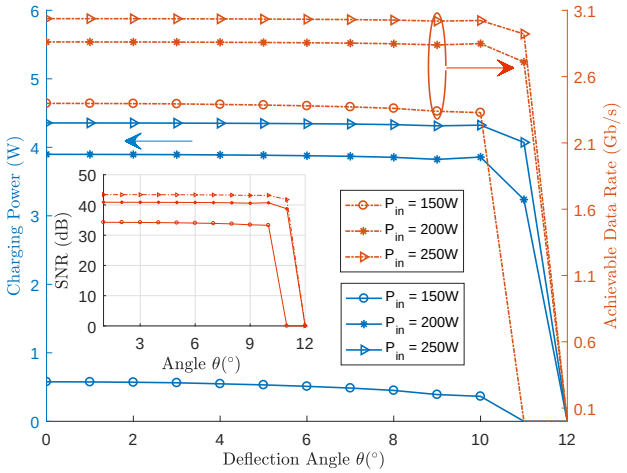

Fig. 14 Charging power and achievable data rate as a function of deflection angle θ with different input power under transmission distance $L = 3$m.

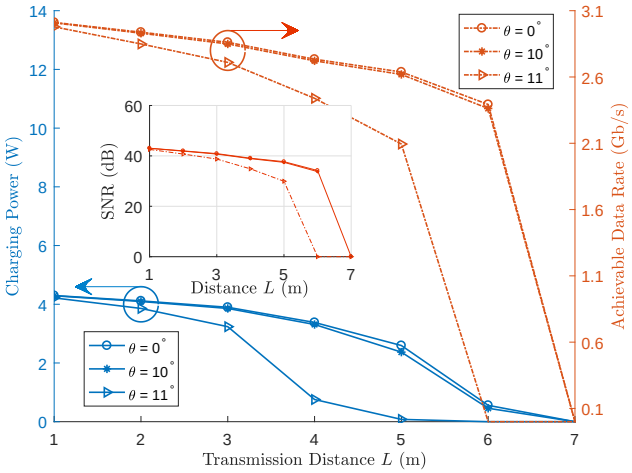

Fig. 13 Charging power and achievable data rate as a function of transmission distance L with different deflection angles under input power $P_{\mathrm{in}} = 200$W.

the conversion efficiency of the PV cell reduces as the incident power increases due to the features of the equivalent circuit model. We also plot the SNR which shows a similar growth trend as the achievable data rate.

Figure 13 depicts the charging power and achievable data rate as a function of transmission distance L with the deflection angle $\theta = 0°, 10°$, and $11°$, and the input power to the system $P_{\mathrm{in}} = 200$W. Evidently, both the energy and data transfer performances reduce with the increase of the transmission distance L. Moreover, L has more impact on the energy transfer than on the data transfer, and as the deflection angle grows, the acceptable transmission distance decreases. Moreover, as illustrated in Fig. 10, the channel gain reduces significantly only as the deflection angle is over $10°$. Thus, there is not much difference between the energy/data transfer performance as $\theta = 0°$ and $\theta = 10°$ and the performance reduces obviously as $\theta = 11°$.

In Fig. 14, we analyze the relationship between the charging power/achievable data rate and the deflection angle θ. The energy/data transfer performance shows a similar tendency with γ as a function of θ. The maximum operational deflection angle between the transceiver with $P_{\mathrm{in}} = 200$W and 250W is $12°$. Moreover, as the input power increases, the charging power grows at a slower rate due to the lower PV conversion efficiency. Furthermore, if the input power is low, there will be no charging power output from the PV.

Additionally, we evaluated the actual data rate and BER of the system using (53) and (54). The length of FFT N is 1024, the cyclic prefix length N_{cp} is 176, and the roll-off factor $\beta = 0.1$. Moreover, the QAM order is 256, i.e., each QAM symbol transmits 8 bit. Thus, the actual data rate reaches 2.6Gb/s according to (53). With this data rate, we obtain that BER $\leq 1.1 \times 10^{-11}$ of the RB-SLIPT system as the input power is 200W within the FOV under transmission distance $L = 3$m according to (54).

D. Discussion

Based on the analytical models, we can analyze the channel gain, charging power, SNR, achievable data rate of the proposed RB-SLIPT system. Moreover, as a mobility-enhanced system, we analyze the performance as a function of moving factors (i.e., moving length and deflection angles) and the largest moving range/FOV of the system is depicted.

The proposed RB-SLIPT system shows the performance of providing more than 4W charging power and more than 3Gb/s capacity with the moving range of 3m and $20°$ FOV under the input power of 250W. However, the end-to-end DC power efficiency is calculated to be around 2%, which in other state-of-the-art laser systems is typically around 10% [7, 8, 16]. We compare the performances of the related SLIPT systems as in Table IV. The proposed system outperforms the other two systems in higher charging power while performs

TABLE IV Performance comparison of SLIPT systems

Scheme	Data rate	Harvested power	End-to-end DC power efficiency	Complexity	Self-alignment
[16]	1.0Gb/s	0.98mW	9.8%	Low complexity	Not support
[10]	1.6Gb/s	40mW	1.2%	Low complexity	Without analysis
Current work	2.6Gb/s	4W	2.0%	High complexity	Support with analysis

poorly in the end-to-end efficiency and implementation complexity. Most importantly, the proposed RB-SLIPT system is capable of positioning mobile receivers with self-alignment characteristic and the mobility analysis is supported.

The efficiency of the electrical power driving the pump LD and the LD pumping the gain medium at the transmitter and the conversion efficiency of PV at the receiver are two key factors restricting the end-to-end efficiency. The conversion efficiency from input electrical power into the RBS to the output laser power is 18%, while the PV conversion efficiency is around 11%. Thus, the end-to-end efficiency can be improved by choosing semiconductor gain medium and PV cell with higher conversion efficiency. The theoretical conversion efficiency for high laser power of the PV cell is up to 40% and the efficiency of semiconductor gain medium is more than 70%. For further reducing the transmission losses (i.e., diffraction loss) over long-distance transmission, optical devices such as lenses and mirrors with larger sizes are supposed to be adopted in the system.

VI. Summary and Conclusions

In this paper, we design an RB-SLIPT system that can deliver multi-Watt power to the mobile receivers with a self-alignment characteristic. We at first establish a mobile transmission channel model to reveal the mobility mechanism and quantitatively evaluate the energy distribution in the channel. Then we propose an exemplary SLIPT design to harvest energy and data using PV and APD respectively. Finally, we analyze the impacts of moving factors on the energy/data transfer performance (charging power and achievable data rate). Numerical analysis illustrates that RB-SLIPT can simultaneously support high charging power, high data rate, and self-positioning mobile receivers within large FOV over long distances. The existing laser-based SLIPT schemes already achieve a high data rate with high energy conversion efficiency. However, the proposed RB-SLIPT is a potential scheme for providing more charging power for various mobile electronics especially in mobile operations.

Several interesting topics are worthy of further investigation in the future: 1) design and analysis for SLIPT with multiple receivers; 2) methods of enhancing deliverable power and data rate; 3) impacts of moving speed on SLIPT stability.

References

[1] K. David and H. Berndt, "6G vision and requirements: Is there any need for beyond 5G?" *IEEE Veh. Technol. Mag.*, vol. 13, no. 3, pp. 72–80, Sept. 2018.

[2] P. D. Diamantoulakis, G. K. Karagiannidis, and Z. Ding, "Simultaneous lightwave information and power transfer (SLIPT)," *IEEE Trans. Green Commun. Netw.*, vol. 2, no. 3, pp. 764–773, Sept. 2018.

[3] M. D. Soltani, M. A. Arfaoui, I. Tavakkolnia, A. Ghrayeb, M. Safari, C. M. Assi, M. O. Hasna, and H. Haas, "Bidirectional optical spatial modulation for mobile users: Toward a practical design for LiFi systems," *IEEE J. Sel. Areas Commun.*, vol. 37, no. 9, pp. 2069–2086, Sept. 2019.

[4] Won-Ho, Shin, Se-Hoon, Yang, Do-Hoon, Kwon, Sang-Kook, and Han, "Self-reverse-biased solar panel optical receiver for simultaneous visible light communication and energy harvesting," *Opt. Express*, vol. 24, no. 22, pp. A1300–A1305, Oct. 2016.

[5] S. Ma, F. Zhang, H. Li, F. Zhou, Y. Wang, and S. Li, "Simultaneous lightwave information and power transfer in visible light communication systems," *IEEE Trans. Wireless Commun.*, vol. 18, no. 12, pp. 5818–5830, Dec. 2019.

[6] A. M. Abdelhady, O. Amin, B. Shihada, and M. Alouini, "Spectral efficiency and energy harvesting in multi-cell SLIPT systems," *IEEE Trans. on Wireless Commun.*, vol. 19, no. 5, pp. 3304–3318, May 2020.

[7] J. Fakidis, S. Videv, H. Helmers, and H. Haas, "0.5-Gb/s OFDM-based laser data and power transfer using a gaas photovoltaic cell," *IEEE Photon. Technol. Lett.*, vol. 30, no. 9, pp. 841–844, May 2018.

[8] J. Fakidis, S. Kucera, H. Claussen, and H. Haas, "On the design of a free space optical link for small cell backhaul communication and power supply," in *2015 IEEE International Conference on Communication Workshop (ICCW)*, London, UK, Jun. 8-12 2015, pp. 1428–1433.

[9] Q. Liu, J. Wu, P. Xia, S. Zhao, W. Chen, Y. Yang, and L. Hanzo, "Charging unplugged: Will distributed laser charging for mobile wireless power transfer work?" *IEEE Veh. Technol. Mag.*, vol. 11, no. 4, pp. 36–45, Dec. 2016.

[10] M. Xiong, Q. Liu, M. Liu, X. Wang, and H. Deng, "Resonant beam communications with photovoltaic receiver for optical data and power transfer," *IEEE Trans. on Commun.*, vol. 68, no. 5, pp. 3033–3041, May 2020.

[11] W. Wang, Q. Zhang, H. Lin, M. Liu, X. Liang, and Q. Liu, "Wireless energy transmission channel modeling in resonant beam charging for IoT devices," *IEEE Internet Things J.*, vol. 6, no. 2, pp. 3976–3986, Apr. 2019.

[12] J. Lim, T. S. Khwaja, and J. Ha, "Wireless optical power transfer system by spatial wavelength division and distributed laser cavity resonance," *Opt. Express*, vol. 27, no. 12, p. A924, June 2019.

[13] G. Zhou, A. J. Alfrey, and L. W. Casperson, "Modes of a laser resonator with a retroreflecting corner cube mirror," *Appl. Opt.*, vol. 21, no. 9, pp. 1670–1674, May 1982.

[14] R. Beer, "Paraxial ray analysis of a cat's-eye retroreflector: comments," *Appl. Opt.*, vol. 15, no. 4, pp. 856–857, Apr. 1976.

[15] Z. Wang, D. Tsonev, S. Videv, and H. Haas, "On the design of a solar-panel receiver for optical wireless communications with simultaneous energy harvesting," *IEEE J. Sel. Areas Commun.*, vol. 33, no. 8, pp. 1612–1623, Aug. 2015.

[16] J. Fakidis, H. Helmers, and H. Haas, "Simultaneous wireless data and power transfer for a 1-Gb/s GaAs VCSEL and photovoltaic link," *IEEE Photon. Technol. Lett.*, vol. 32, no. 19, pp. 1277–1280, Aug. 2020.

[17] M. S. Islim, R. X. Ferreira, X. He, E. Xie, S. Videv, S. Viola, S. Watson, N. Bamiedakis, R. V. Penty, I. H. White, A. E. Kelly, E. Gu, H. Haas, and M. D. Dawson, "Towards 10Gb/s orthogonal frequency division multiplexing-based visible light communication using a gan violet micro-led," *Photon. Res.*, vol. 5, no. 2, pp. A35–A43, Apr. 2017.

[18] G. Pan, J. Ye, and Z. Ding, "Secure hybrid VLC-RF systems with light energy harvesting," *IEEE Trans. on Commun.*, vol. 65, no. 10, pp. 4348–4359, Oct. 2017.

[19] Y. Li, N. Huang, J. Wang, Z. Yang, and W. Xu, "Sum rate maximization for VLC systems with simultaneous wireless information and power transfer," *IEEE Photon. Technol. Lett.*, vol. 29, no. 6, pp. 531–534, Mar. 2017.

[20] A. E. Siegman, *Lasers*. University Science Books, 1986.

[21] O. E. Martinez, "Matrix formalism for dispersive laser cavities," *IEEE J. Quantum Electron.*, vol. 25, no. 3, pp. 296–300, Mar. 1989.

[22] N. Hodgson and H. Weber, *Laser Resonators and Beam Propagation: Fundamentals, Advanced Concepts, Applications*, ser. Springer Series in Optical Sciences. Springer Berlin Heidelberg, 2005, vol. 108.

[23] J. A. Hudson, "Fresnel-Kirchhoff diffraction in optical systems: An approximate computational algorithm," *Appl. Opt.*, vol. 23, no. 14, pp. 2292–2295, July 1984.

[24] F. Shen and A. Wang, "Fast-fourier-transform based numerical integration method for the rayleigh-sommerfeld diffraction formula," *Appl. Opt.*, vol. 45, no. 6, pp. 1102–1110, Feb. 2006.

[25] M. Shen, S. Wang, L. Hu, and D. Zhao, "Mode properties produced by a corner-cube cavity," *Appl. Opt.*, vol. 43, no. 20, pp. 4091–4094, Apr. 2004.

[26] A. G. Fox and T. Li, "Resonant modes in a maser interferometer," *The Bell System Technical Journal*, vol. 40, no. 2, pp. 453–488, Mar. 1961.

[27] M. H. Weik, *Gaussian beam*. Boston, MA: Springer US, 2001, pp. 675–675. [Online]. Available: https://doi.org/10.1007/1-4020-0613-6_7895

[28] J. Armstrong, "OFDM for optical communications," *J. Lightw. Technol.*, vol. 27, no. 3, pp. 189–204, Feb. 2009.

[29] Y. A. Bachtiar and T. Adiono, "PAM-4 modulator-demodulator design modeling for visible light communication (VLC)," in *2019 International Symposium on Electronics and Smart Devices (ISESD)*, Badung, Indonesia, Oct. 8-9 2019, pp. 1–5.

[30] J. Ma, J. He, J. Shi, J. He, Z. Zhou, and R. Deng, "Nonlinear compensation based on k-means clustering algorithm for Nyquist PAM-4 VLC system," *IEEE Photon. Technol. Lett.*, vol. 31, no. 12, pp. 935–938, May 2019.

[31] M. S. Demir, F. Miramirkhani, and M. Uysal, "Handover in VLC networks with coordinated multipoint transmission," in *2017 IEEE International Black Sea Conference on Communications and Networking (BlackSeaCom)*, Istanbul, Turkey, June 5-8, 2017, pp. 1–5.

[32] J.-m. Liu, *Semiconductor lasers and light-emitting diodes*. Cambridge University Press, 2005, pp. 816–925.

[33] B. R. Strickland, M. J. Lavan, E. Woodbridge, and V. Chan, "Effects of fog on the bit-error rate of a free-space laser communication system," *Appl. Opt.*, vol. 38, no. 3, pp. 424–431, Jan. 1999.

[34] M. J. N. Sibley, *Optical communications : components and systems*. Macmillan, 1995.

[35] B. Clerckx, "Waveform optimization for SWIPT with nonlinear energy harvester modeling," in *WSA 2016, 20th International ITG Workshop on Smart Antennas*, Munich, Germany, Mar. 9-11 2016, pp. 1–5.

[36] L. . Fock, A. Kwan, and R. S. Tucker, "Reduction of semiconductor laser intensity noise by feedforward compensation: experiment and theory," *J. Lightw. Technol.*, vol. 10, no. 12, pp. 1919–1925, Dec. 1992.

[37] F. Xu, M. Khalighi, and S. Bourennane, "Impact of different noise sources on the performance of pin- and APD-based FSO receivers," in *Proceedings of the 11th International Conference on Telecommunications*, Graz, Austria, June 15-17, 2011, pp. 211–218.

[38] D. Tsonev, H. Chun, S. Rajbhandari, J. J. D. McKendry, S. Videv, E. Gu, M. Haji, S. Watson, A. E. Kelly, G. Faulkner, M. D. Dawson, H. Haas, and D. O'Brien, "A 3-Gb/s single-LED OFDM-based wireless VLC link using a gallium nitride μLED," *IEEE Photon. Technol. Lett*, vol. 26, no. 7, pp. 637–640, Jan. 2014.

[39] A. Lapidoth, S. M. Moser, and M. A. Wigger, "On the capacity of free-space optical intensity channels," *IEEE Trans. Inf. Theory*, vol. 55, no. 10, pp. 4449–4461, Oct. 2009.

[40] S. Ma, R. Yang, Y. He, S. Lu, and S. Li, "Achieving channel capacity of visible light communication," *IEEE Syst. J.*, vol. PP, no. 99, pp. 1–12, May 2020.

[41] S. Ma, R. Yang, H. Li, Z. Dong, H. Gu, and S. Li, "Achievable rate with closed-form for SISO channel and broadcast channel in visible light communication networks," *J. Lightw. Technol.*, vol. 35, no. 14, pp. 2778–2787, May 2017.

[42] P. Crump, W. Dong, M. Grimshaw, J. Wang, S. Patterson, D. Wise, M. DeFranza, S. Elim, S. Zhang, M. Bougher, J. Patterson, S. Das, J. Bell, J. Farmer, M. DeVito, and R. Martinsen, "100-W+ diode laser bars show $>$ 71% power conversion from 790- nm to 1000-nm and have clear route to $>$ 85%," in *Proc. of SPIE*, ser. Society of Photo-Optical Instrumentation Engineers (SPIE) Conference Series, vol. 6456, 2007, p. 64560M.

[43] MHGoPower, "Photovoltaic Converter YCH-H6424

Datasheet," http://www.mhgopower.com/images/YCH-H6424_15V_PPC_Datasheet_Rev_2.3_03-12-2020.pdf Accessed Feb. 4, 2021.

[44] M. Perales, M.-h. Yang, C.-l. Wu, C.-w. Hsu, W.-s. Chao, K.-h. Chen, and T. Zahuranec, "Characterization of high performance silicon-based VMJ PV cells for laser power transmission applications," in *High-Power Diode Laser Technology and Applications XIV*, ser. Society of Photo-Optical Instrumentation Engineers (SPIE) Conference Series, M. S. Zediker, Ed., vol. 9733, Mar. 2016, p. 97330U.